minerals

Article

Zircon U–Pb Geochronology, Geochemistry and Geological Significance of the Santaishan–Yingjiang Ultramafic Rocks in Western Yunnan, China

Huimin Liu [1], Yongqing Chen [1,*] and Zhi Shang [2]

[1] School of Earth Sciences and Resources, China University of Geosciences Beijing, Beijing 100083, China; hmliu0302@163.com

[2] Department of Emergence Rescue, China Fire and Rescue Institute, Beijing 102201, China

* Correspondence: 2006012078@cugb.edu.cn

Abstract: The study of ultramafic rocks in Western Yunnan is of great significance for an understanding of the tectonic evolution of the Neo-Tethys Ocean. The zircon U–Pb data indicated that the Santaishan serpentinized pyroxene peridotite (SSPP) was formed 186–190 Ma, and the Yingjiang hornblende pyroxenite (YHP) was formed 182–183 Ma. The content of MgO in the SSPP is relatively high, but the SiO_2, Al_2O_3, CaO and TiO_2 content and ΣREE are low, while the YHP has opposite characteristics. The samples from the SSPP and YHP have similar distribution patterns of trace elements, both being enriched in large ion lithophile elements (LILEs) such as Rb, Ba and Th and depleted in high field strength elements (HFSEs) such as Ti, P and Nb. These characteristics are consistent with the supra-subduction zone (SSZ) type and mid-ocean ridge basalt (MORB) type of ophiolite in the Bangong–Nujiang suture zone. The SSPP rocks have relatively high $(^{87}Sr/^{86}Sr)_i$ ratios (0.7091–0.7131) and positive Hf(t) values (11.2–13.8), with εNd(t) values varying from −1.1 to 9.4. The YHP has relatively low εHf(t) values (3.5 to 6.9), with the Nd–Hf isotopic model ages ranging from 610 to 942 Ma. The signatures of Sr–Nd and Lu–Hf isotopes indicate that the SSPP and YHP were derived from the depleted mantle, and the crustal material in the magma source may have originated from the Neoproterozoic Rodinia supercontinent. In the early Middle Jurassic (190 Ma), the Tengchong Block was in the setting of an active continental margin induced by the subduction of the Bangong–Nujiang Ocean, where the SSZ-type SSPP with ophiolite characteristics was formed. With the continuous subduction of the Bangong–Nujiang Ocean, the slab retreated and induced mantle convection, which resulted in the gradual thinning of the continental crust. Meanwhile, the Yingjiang back-arc basin was formed 183 Ma. Under the influence of the upwelling of the asthenosphere and the mixture of crustal materials, the MORB-type YHP was formed.

Keywords: western Yunnan; ultramafic rock; Bangong–Nujiang suture zone; zircon U–Pb age; Neo-Tethys Ocean

check for updates

Citation: Liu, H.; Chen, Y.; Shang, Z. Zircon U–Pb Geochronology, Geochemistry and Geological Significance of the Santaishan–Yingjiang Ultramafic Rocks in Western Yunnan, China. *Minerals* **2023**, *13*, 536. https://doi.org/10.3390/min13040536

Academic Editors: Fernando Velasco-Tapia, Juan Alonso Ramírez Fernández and Uwe Jenchen

Received: 3 March 2023
Revised: 31 March 2023
Accepted: 10 April 2023
Published: 12 April 2023

1. Introduction

The Tethys tectonic domain, with a total length of about 15,000 km, starts from northeastern Australia in the east; crosses successively to southeast Asia, the Indo-Myanmar Mountains, the southern Qinghai–Tibet Plateau and the Iranian Plateau; and ultimately extends to western Europe through the Mediterranean Sea [1]. The Tethys tectonic domain has attracted substantial attention because of its abundant geological phenomena and mineral resources. A systematic study of it may not only reveal the evolutionary history of the crust but also guide exploration for mineral resources [2–7].

On the basis of plate tectonics, previous works have proposed a division of the Paleo-Tethys and Neo-Tethys Oceans and argued that the southern subduction of the Paleo-Tethys Ocean led to the splitting and expansion of the northern margin of the Gondwana continent, resulting in the formation of the Neo-Tethys Ocean. In China, the Neo-Tethys Ocean is composed of two main ocean basins, the Bangong–Nujiang Ocean and the Yarlung Tsangpo Ocean [1–3]. The Tengchong Bloc is located between the Yarlung Tsangpo suture zone and the Bangong-Nujiang suture zone, which is the southern extension of the Lhasa Block. It is separated from the Baoshan Block by the Nujiang fault in the east and connects with the Burma Block along the Myitkyina ophiolite belt in the west (Figure 1) [8–11]. The Bangong–Nujiang ophiolite belt is cut by the Karakoram fault at its westernmost and passes eastward from Bangong Lake to Gaize, Dingqing and other places in Tibet. Thereafter, the Bangong–Nujiang ophiolite belt enters Yunnan, which is covered by the Gaoligong thrust belt, and finally arrives in northern Myanmar and extends into the Andaman Sea along the Saging fault [12,13]. The exact subduction time of the Bangong–Nujiang Ocean is still controversial. Qiu et al. believed that the Bangong–Nujiang Ocean began to subduct southward in the Middle Jurassic and closed in the Early Cretaceous [14]. Mo et al. supposed that the opening time of the Neo-Tethys Ocean should be at the Late Triassic or earlier, the subduction started before 170 Ma, and the closure time might be in the Late Jurassic (ca. 159 Ma) to the end of the Early Cretaceous (ca. 99 Ma) [3]. With the closure of the Neo-Tethys Ocean, the Lhasa Block collided with the Qiangtang Block. Shi et al. studied Bangong Lake's ophiolite and found that the maximum age of the gabbro was 177 Ma, suggesting that the subduction of the Bangong–Nujiang Ocean was earlier than 177 Ma [15].

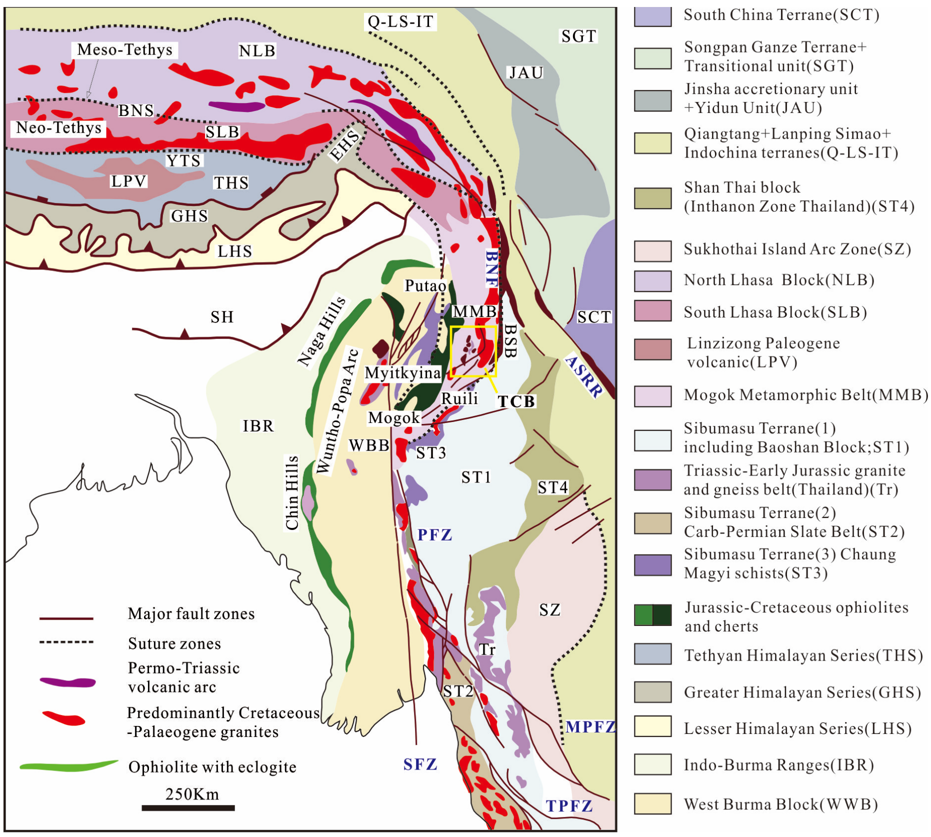

Figure 1. Simplified geological map of the Eastern Tethys (modified from [16]). Abbreviations: BNS—Bangong-Nujiang Suture; YTS—Yarlung Tsangpo Suture; BSB—Baoshan Block; BNF—Bangong–Nujiang Fault; ASRR—Ailao Shan–Red River shear zone; SCT—South China Terrane; EHS—Eastern Himalayan Syntaxis; SH—Shillong plateau; SFZ—Sagaing Fault Zone; TPFZ—Three Pagodas Fault Zone; MPFZ—Mae Ping Fault Zone; PFZ—Paung Laung Fault Zone.

Small amounts of ultramafic rock are exposed in Santaishan Village, Tengchong Block, and the rocks are generally serpentinized. Previous studies have had different understandings of the genesis and tectonic settings of the ultramafic rocks in Santaishan. The attribution of the ultramafic rocks in the Santaishan has always been controversial, with the main viewpoints being that (1) they are remnants of the oceanic lithospheric mantle, (2) they belong to the ancient continental basement and (3) they are part of the Bangong–Nujiang ophiolite belt. The Yunnan Bureau of Geology and Mineral Resources Exploration found that the Middle Jurassic coarse clastic rocks exposed around the Santaishan ultramafic rocks contained chromite fragments, indicating that the Santaishan ultramafic rocks were formed before the Middle Jurassic. Zhang et al. believed that the ultramafic rocks in Santaishan were formed in the Late Triassic to Early Jurassic and experienced strong tectonic deformation [12]. Zhong et al. supposed that there was no ophiolite in Santaisan because no record of an oceanic crust was found in this area [8,17]. Liu et al. believed that the Santaishan ultramafic rocks may represent rootless ophiolite fragments, and the Longling–Ruili fault represents the suture zone between the Tengchong and Baoshan Blocks [18]. Through Os isotope studies, Chu et al. concluded that the Santaishan ultramafic rocks were derived from the enriched lithospheric mantle, rather than part of the Bangong–Nujiang ophiolite belt [13]. Wang et al. speculated that the peridotite underwent 25%–35% partial melting at the mid-ocean ridge in the early stage and was modified by the subducted oceanic crust, which has similar characteristics to the ophiolite in the Yarlung Tsangpo suture zone [19].

Previous studies on ultramafic rocks in western Yunnan have mainly focused on Santaishan and have defined the evolution of the Neo-Tethys Ocean through isotopic chronology studies. However, systematic studies on the magma sources, petrogenesis, and the formation of the tectonic setting of these ultramafic rocks are still scarce, although these are vital to understanding the evolution of western Yunnan [12–19].

In this study, a small number of ultramafic rock outcrops were found in Luluo Village, Yingjiang County, and there has been no systematic research on them. We assumed that there is some degree of relationship between the ultramafic rocks of Santaishan and Yingjiang in western Yunnan, which is of great significance for understanding the evolution of the Neo-Tethys Ocean. On the basis of a detailed field geological survey and previous studies, the ultramafic rocks of the two regions were systematically studied through zircon U–Pb dating, whole-rock geochemical analysis, zircon Hf isotope analysis and whole-rock Sr–Nd isotope analysis to define the formation of these ultramafic rocks and the evolution of the Neo-Tethys Ocean in the Middle Jurassic.

2. Geologic Background and Petrography

The western Yunnan experienced frequent tectono-magmatic activities and has a complex geological background. The strata, structures and magmatic rocks in this region are arc-shaped. The main tectonic zones from west to east are Binlangjiang fault (BJF), Dayingjiang–Guyong fault (DGF), Qipanshi–Tengchong fault (QTF) and Bangong–Nujiang fault (BNF) (Figure 2), and the sedimentary strata outcrops are mainly a series of Late Paleozoic and Early Mesozoic carbonates and clastic rocks. The crystalline basement of the Tengchong Block is composed of the Paleoproterozoic Gaoligong Mountain Group, which consists of amphibolite, feldspathic gneisses, quartzite, migmatite and marble [20]. The Early Paleozoic strata are dominated by the lower Ordovician carbonate rocks and miss the middle to upper Ordovician and Silurian strata. The Late Paleozoic strata are a set of clastic and carbonate rocks formed in a continental margin environment, and the Devonian–Permian is mainly clastic rocks containing minor basic volcanic and carbonate rocks, which were covered by Mesozoic and Cenozoic volcanic activity. The Mesozoic strata are less distributed and were mainly deposited in the Triassic and Middle Jurassic; their lithology is composed of clastic rocks and limestone. The lithology in the Cenozoic is complex, including coal-bearing clastic rocks and conglomerates, pyroclastic rocks and a small amount of basic to intermediate volcanic rocks [20].

There have been four periods of magmatic activity: the Cambrian–Ordovician, Triassic–Early Jurassic, Early Cretaceous and Late Cretaceous–Early Palaeogene [20–22]. Ultramafic rocks are mainly distributed in Luxi and Yingjiang. The SSPP is located at the western margin of the Nujiang–Bangong–Ruili fault, occurring as a lens-like shape in the NEE direction along the shear zone. The SSPP is in fault contact with the Jurassic–Cretaceous red thick layer of clastic rocks. The YHP is distributed near the BJF and has an intrusion relationship with the Cenozoic volcanic rocks. The ultramafic rock samples in this study were collected from Santaishan Village in Luxi County and Luluo Village in Yingjiang County (Figure 2).

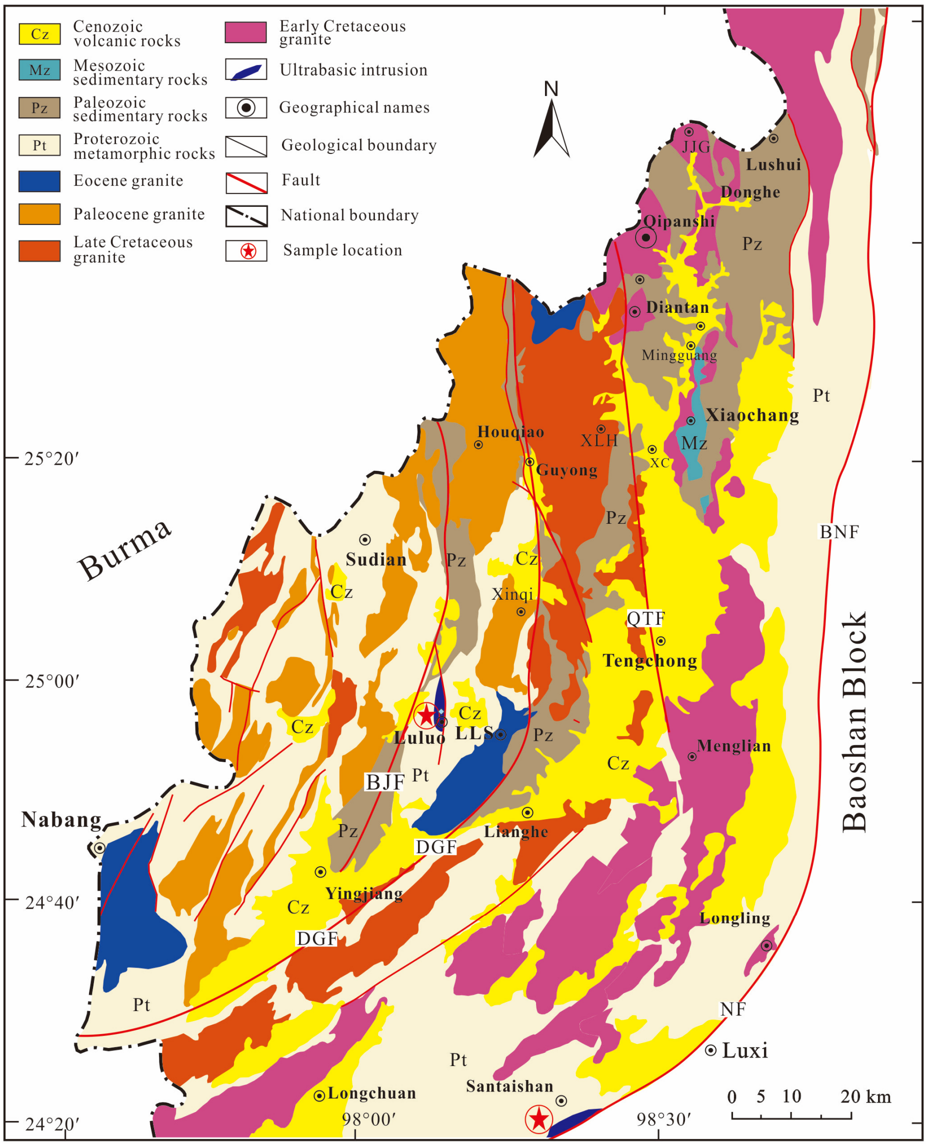

Figure 2. Simplified geological map showing the major geologic units of the Tengchong Block (TCB), the spatial-temporal distribution of the ultramafic and sample localities in this study (modified from [16]). Abbreviations: BNF—Bangong–Nujiang Fault; QTF—Qipanshi–Tengchong Fault; DGF—Dayingjiang–Guyong Fault; BJF—Binlangjiang Faul.

The SSPP rocks have a vein-like appearance and a grayish-to-black color (Figure 3a). The main mineral composition is olivine and pyroxene, with spinel as a secondary mineral. The rocks exhibit lamellar and massive structures (Figure 3b). Olivine content accounts for about 65% of the total mineral, and its highest interference color is grade III green. The serpentinization of the olivine along the cleavage. A small amount of magnetite is the product of olivine dissociation during serpentinization. Pyroxene accounts for about 25% of the total mineral content, with the main grain size being 0.5–2 mm. Bastite takes the place of pyroxene and assumes its appearance with a metasomatic structure. Spinel makes up about 2% of the total minerals; the main particle size is 0.2–0.5 mm (Figure 4a,b). Strong serpentinization and sericitization are obvious in the rocks. Therefore, we supposed that the original rock was pyroxene peridotite, and, under the subsequent metamorphism, the peridotite and pyroxene strongly metamorphosed into serpentine, presenting a metasomatic structure.

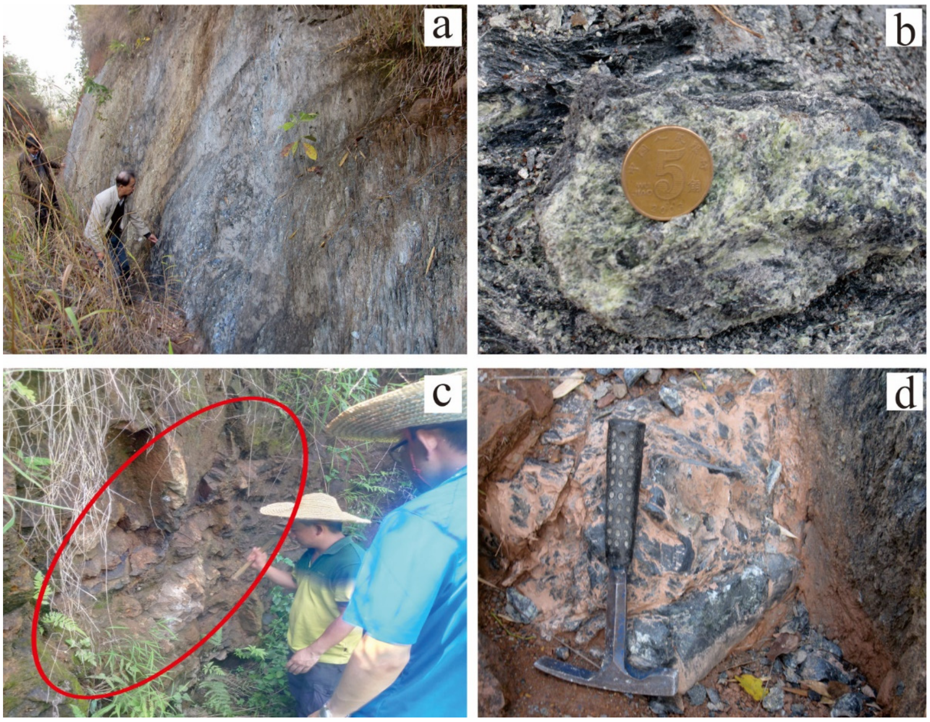

Figure 3. Santaishan ultramafic outcrops and hand specimens (**a**,**b**), Yingjiang ultramafic outcrops and hand specimens (**c**,**d**).

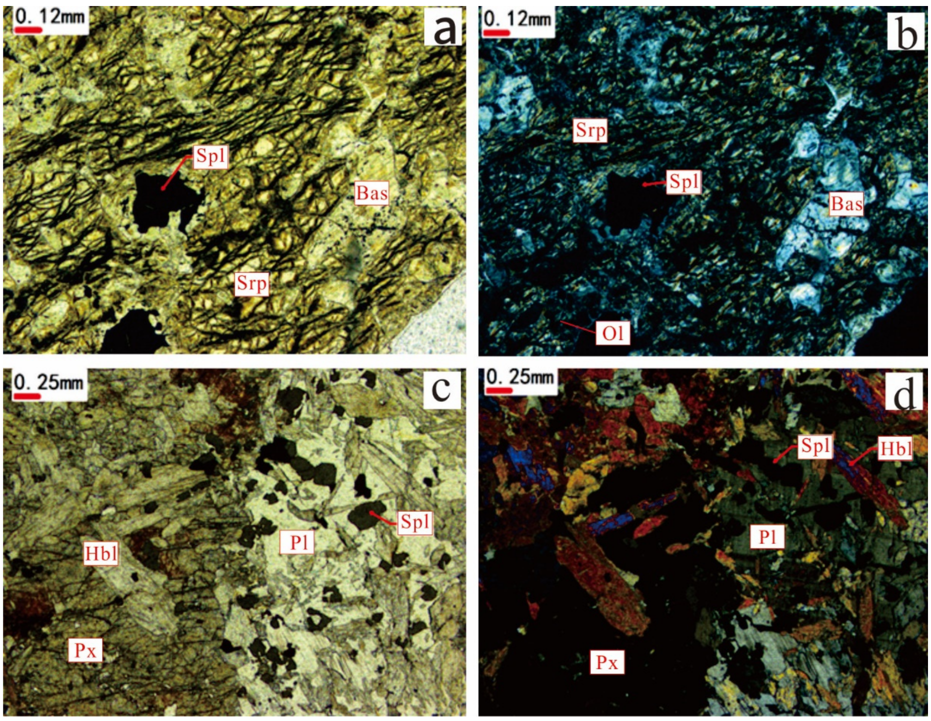

Figure 4. Single-polarized (**a**,**c**), cross-polarized (**b**,**d**). Light photomicrographs of ultramafic rocks in Santaishan (**a**,**b**) and Yingjiang (**c**,**d**). Px—pyroxene, Pl—plagioclase, Hbl—hornblende, Ol—olivine, Spl—spinel, Bas—Bastite, Srp—serpentine.

The YHP rocks have a vein-like occurrence with a weak alteration. The fresh rocks are gray-green, with high hardness (Figure 3c). Most pyroxene and hornblende can be observed in hand specimens. The rocks have a hypidiomorphic granular texture and a massive structure (Figure 3d). The main mineral components are pyroxene and hornblende. The secondary minerals are spinel and plagioclase. The pyroxene content is about 60%, for which the main particle size is 0.5–2 mm. This is mainly clinopyroxene pyroxene, followed by orthopyroxene. Orthopyroxene precipitates iron oxides to various degrees. Hornblende makes up 25% of the total minerals and has a principal grain size of 0.5–2 mm. The content of plagioclase is about 7%, and it often contains hornblende, spinel and magnetite inclusions. The content of spinel accounts for about 6% of the total minerals and is filled between pyroxene and hornblende grains; the main particle size is 0.1–0.5 mm (Figure 4c,d). The Yingjiang ultramafic rocks contain clinopyroxene, indicating that the degree of melting was lower than that of the Santaishan ultramafic rocks without clinopyroxene.

3. Methods

3.1. Sample Collection

On the basis of detailed field profile observations, fresh rock samples were collected at fixed points along the profiles. The coordinates of where the Santaishan ultramafic rocks were sampled are 24°20′33″ N, 98°23′35″ E, and 20 samples in total were collected. The coordinates of where the ultramafic rocks from Yingjiang were sampled are 24°56′18.61″ N, 98°7′44.79″ E, and 6 samples were collected in total. After the sampling was completed, a system was organized, including classification labels, cleaning and taking photographs.

3.2. LA–ICP–MS Analyses of Zircon

Twenty-eight kilograms of fresh ultramafic rocks were collected to extract the zircons. The surface of the sample was first washed clean with water and dried naturally. Then we crushed the sample to pass through an 80-mesh sieve. After coarse washing with water, strong magnetic separation, electromagnetic separation and fine washing with alcohol, the zircons were hand-picked under a double microscope.

U–Pb analyses of the zircon were conducted at the Laboratory of Continental Dynamics, Institute of Geology, Chinese Academy of Geological Sciences. The abundance of U–Pb was measured using the latest Neptune Plus multiple collectors (ICP-MS) from Thermo Fisher Co., Ltd., Waltham, MA, USA. The laser ablation system used in the measurement was the GeoLasPro 193 nm system developed by U.S. Coherent Co., Ltd., Santa Clara, CA, USA. Helium was used as a carrier gas to enhance the efficient transport of the ablated material. The spot size of the laser ablation beam was 25 μm. The LA-ICP-MS operating conditions were optimized on the basis of measurements of the reference material, zircon 91,500. The accuracy of the data was verified by using GJ-1 as an auxiliary standard. The LA-ICP-MS measurements were carried out using a time-resolved analysis operated in fast peak-hopping and DUAL detector mode with a short integration time. The Harvard standard zircon 91,500 and GJ-1 were measured after every 5–10 samples to ensure no drift was occurring. The data were analyzed in the ICPMSDataCal program [23] and the Isoplot program [24].

3.3. Lu–Hf Isotopic Analyses of Zircon

The Lu–Hf isotope test of zircon was completed at the Continental Dynamics Laboratory of the Institute of Geology, Chinese Academy of Geological Sciences, and the Lu–Hf isotope test was based on the zircon U–Pb age, using a multi-receiver plasma mass spectrometry instrument (Neptune) and a laser ablation system (LA-MC-ICP-MS). We also performed a secondary test on the origin of the zircon U–Pb microregion. The carrier gas of the ablative material used in the Continental Dynamics Laboratory was the rare gas He, the diameter of ablation was 30 μm, and the international general zircon standard GJ-1 was used as the standard reference for calibration [25].

3.4. Major and Trace Element Analyses

The bulk-rock major and trace element compositions of the samples were measured at the Testing Center of Rocks and Minerals in Henan province. The major elements were analyzed using a ZSX100e X-ray fluorescence spectrometer (XRF) on fused glass beads. The trace elements, including rare earth elements, were measured by inductively coupled plasma mass spectrometry (ICP-MS) with an XSERIES2 instrument. Details of the methodology of the analytical procedures can be found in Gao [26]. The analyses of the international standards returned values that agreed with their published values. Analyses of the international rock standards indicated that the precision and accuracy were better than 1.5% for all elements.

3.5. Whole-Rock Sr–Nd Isotopic Analyses

The Sr–Nd isotope analyses were carried out at the Laboratory of Tianjin Institute of Geology and Mineral Resources, Ministry of Land and Resources. Powdered bulk-rock samples were first spiked with mixed isotope tracers and then dissolved in a solution of HF and HNO_3 in Teflon capsules before undergoing Rb–Sr and Sm–Nd isotope analyses. Rb, Sr, Sm and Nd were separated using conventional ion exchange procedures, as described by Yan [27]. The Sr–Nd isotopic data were measured on a VG Axiom mass spectrometer. The Nd and Sr ratios were normalized to $^{146}Nd/^{144}Nd$ = 0.7219 and $^{86}Sr/^{88}Sr$ = 0.1194, respectively. The BCR-2 standards, which were $^{143}Nd/^{144}Nd$ = 0.512633 ± 0.000017 (2σ) and $^{87}Sr/^{86}Sr$ = 0.705013 ± 0.000019 (2σ), respectively, were used to assess the analytical precision.

4. Results

4.1. Zircon U–Pb Dating

In this study, two samples were selected separately from the SSPP and YHP for zircon dating. The data for the YHP are listed in Table S3, and the data for the SSPP are listed in Table S7. Zircons in the SSPP mainly had a broad tabular shape, with elongation ratios ranging from 1:1 to 2:1. In the cathodoluminescence diagram, the zircon grains were gray-black with low transparency. Some zircons had clear oscillating zoning, implying a magmatic origin (Figure 5a,c). Zircons in the YHP mainly had a broad plate-like shape, with lengths of 60–180 μm, a width of 40–100 μm and elongation ratios ranging from 1.2:1 to 2:1. In the cathodoluminescence diagram, the zircon grains were gray with high transparency. Explicit oscillating zoning could be seen in some of the zircon grains, and no inherited cores were seen (Figure 5e,g).

The Th and U contents of zircons in the SSPP were 247.5–3964.3 ppm and 701.3–3043.6 ppm, respectively, with Th/U ratios ranging from 0.26 to 1.95. Thirteen spots of Sample STS-01 were analyzed, and the $^{206}Pb/^{238}U$ ages ranged from 180.1 to 188.2 Ma (Figure 4b), with a weighted mean age of 186.2 ± 2.3 Ma (MSWD = 0.15). The $^{206}Pb/^{238}U$ ages of 35 spots in Sample STS-02 ranged from 184.1 to 195.7 Ma (Figure 5d), with a weighted mean age of 190.5 ± 1.3 Ma (MSWD = 0.57).

The Th and U contents of zircons in the YHP samples ranged from 23.0 to 4556.0 ppm and 53.3 to 1890.5 ppm, respectively, with Th/U ratios varying from 0.22 to 2.41. Sample YJLL-01 had $^{206}Pb/^{238}U$ ages ranging from 175.1 to 190.2 Ma in 32 spots (Figure 5f), with a weighted mean age of 183.7 ± 1.8 Ma (MSWD = 0.7). The $^{206}Pb/^{238}U$ ages in 32 spots of Sample YJLL-02 ranged from 173.8 to 189.4 Ma (Figure 5h), with a weighted mean age of 182.0 ± 1.4 Ma (MSWD = 1.06).

All of the $^{232}Th/^{238}U$ ratios were greater than 0.1. Combined with the development of oscillating zonal zones on the zircon's structure and CL image analysis, it could be shown that these zircons were all magmatic zircons. The high content of Th and U may have been caused by alterations.

In conclusion, almost all the ages of single zircon grains are in accordance with the concord line and are relatively concentrated, indicating that the U–Pb system of these zircons remained closed after their formation. The rocks of the SSPP and YHP were formed 186.2–190.5 Ma and 182.0–183.7 Ma, respectively.

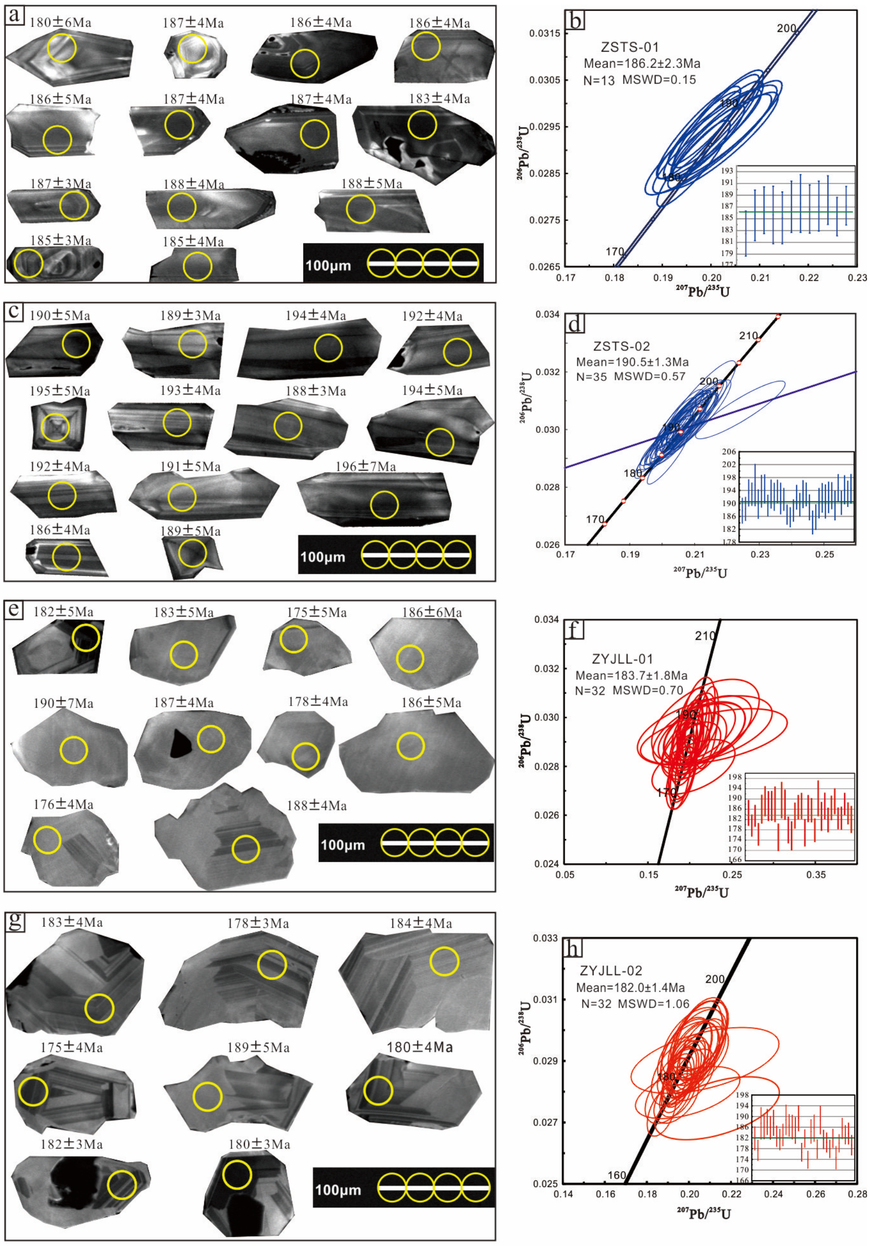

Figure 5. CL images of representative zircon grains (**a**,**c**,**e**,**g**), zircon U–Pb Concordia diagrams (**b**,**d**,**f**,**h**).

4.2. Lu–Hf Isotopic Analyses of Zircon

On the basis of the zircon U–Pb dating, one sample from the SSPP and two samples from the YHP were used for Lu–Hf isotope analyses, referring to the CL image. The data for the YHP are listed in Table S4, and the data for the SSPP are listed in Table S8. The initial Hf isotopic ratios for all the samples were corrected to their zircon U–Pb ages.

Fourteen spots were tested for Sample STS-01 of the SSPP. The results were as follows: $^{176}Yb/^{177}Hf$ = 0.016427–0.159872; $^{176}Lu/^{177}Hf$ = 0.000620–0.005208; initial $^{176}Hf/^{177}Hf$ = 0.282559–0.282722; εHf(t) = 11.2–13.8. The single-stage Hf model ages of zircon (T_{DM1}) ranged from 268 to 375 Ma.

Thirty-two spots of Sample YJLL-01 from the YHP were tested. The $^{176}Yb/^{177}Hf$, $^{176}Lu/^{177}Hf$ and initial $^{176}Hf/^{177}Hf$ ratios were 0.001985–0.016247, 0.000081–0.000492 and 0.282773–0.282865, respectively. The T_{DM1} ages ranged from 535 to 664 Ma, with the εHf(t) values varying from 3.6 to 6.9. The results for Sample YJLL-02 in 31 spots were as follows: $^{176}Yb/^{177}Hf$ = 0.002010–0.010545; $^{176}Lu/^{177}Hf$ = 0.000091–0.000456; εHf(t) = 3.5–6.5; initial $^{176}Hf/^{177}Hf$ = 0.282772–0.282854. The T_{DM1} ages ranged from 552 to 667 Ma.

4.3. Whole-Rock Geochemistry

Eight samples from the YHP and 20 samples from the SSPP were used for whole-rock analyses. The results are listed in Tables S1 and S5. The analyses of the mineral composition of the CIPW standard are listed in Tables S2 and S6. All the samples had a low oxide content, a high mafic content and a low total alkali content. The SSPP showed strong alteration with a high loss on ignition (LOI) (12%–15%). The LOI of the YHP was low (1.18–2.62%, the average value was 1.86%), indicating that the samples were fresh. In order to eliminate the effect of the alteration on the original components and to facilitate comparison, the normalized values after deducting the volatile components are used to discuss the main elements. In the TAS diagram of igneous rocks (Figure 6a), the samples from the SSPP and YHP were distributed in the Picrite basalt area. In the TFeO/MgO-SiO_2 diagram (Figure 6b), the YHP samples were distributed in the tholeiitic series, and the SSPP samples were distributed in the calc-alkaline series.

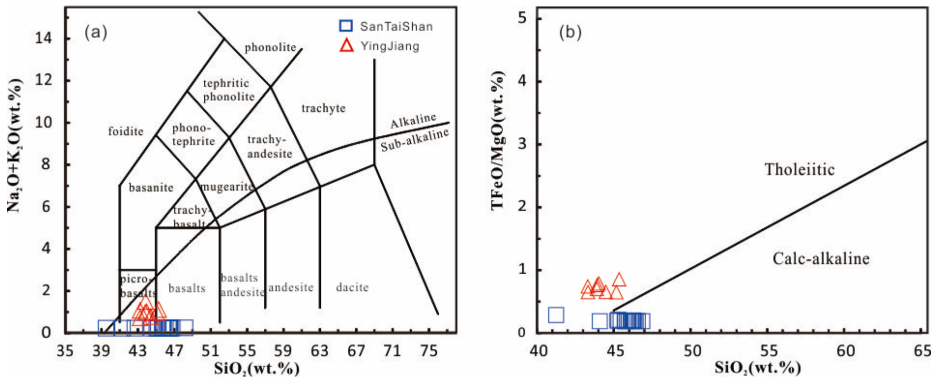

Figure 6. (**a**) SiO_2–Na_2O + K_2O diagram (modified from [28]); (**b**) SiO_2–TFeO/MgO diagram (modified from [29]).

The content of MgO (37.57–45.06 wt.%) in the SSPP samples was relatively high, but the content of SiO_2 (39.42–46.80 wt.%), Al_2O_3 (0.40–10.53 wt.%), CaO (0.07–3.49 wt.%), TiO_2 (0.001–0.126 wt.%), TFe_2O_3 (7.39–11.37 wt.%), MnO (0.12–0.20 wt.%) and P_2O_5 (0.007–0.013 wt.%) was low. In contrast, the content of MgO (23.62–27.43 wt.%) in the YHP samples was relatively low, but the content of SiO_2 (43.25–45.29 wt.%), Al_2O_3 (3.89–4.65 wt.%), CaO (2.45–4.84 wt.%), TiO_2 (0.92–1.15 wt.%), TFe_2O_3 (16.90–19.85 wt.%), MnO (0.20–0.28 wt.%) and P_2O_5 (0.019–0.056 wt.%) was high.

The total rare earth elements (ΣREE) in the SSPP samples (1.14–10.65 ppm) were much lower than that in the YHP samples (28.19–174.86 ppm). The ratios of LREE/HREE (5.88–14.28) and $(La/Yb)_N$ (4.26–15.74) in the SSPP samples were higher than those in the YHP samples (LREE/HREE = 2.22–2.93, $(La/Yb)_N$ = 1.49–5.28). In the chondrite-normalized diagram of REE (Figure 7a), the SSPP rocks showed a U-type enriched curve, while the YHP rocks exhibited a flat distribution. $\delta Eu = Eu/Eu^* = 2 \times Eu/(Sm + Gd)$ is calculated based on the Akimasa-Collier diagram, where Eu, Sm and Gd are all standardized values for chondrites. The δEu values of the SSPP rocks were 0.26–3.85, showing negative to positive Eu anomalies, while the δEu values in the YHP rocks varied from 0.98 to 1.80 (mean: 1.31), and the Eu anomaly was not obvious. The $(La/Sm)_N$ and $(Gd/Yb)_N$ values in the SSPP rocks were 5.06–11.37 and 0.7–2.9, respectively, showing obvious differentiation of the LREE and inconspicuous differentiation of the HREE. The differentiation of LREE and HREE in the YHP rocks was not significant, with the $(La/Sm)_N$ ratios varying from 1.63 to 4.27 and the $(Gd/Yb)_N$ ratios ranging from 1.05 to 1.73. In the primitive-mantle-normalized trace element diagram (Figure 7b), large ion lithophile elements (LILEs) such as Rb, Ba and Th were enriched in the SSPP and YHP, while high field strength elements (HFSEs) such as Ti, P, U and Nb were depleted. Strong K, P and Ti negative anomalies are displayed by the majority of the ultramafic rocks. The K anomaly could be related to the rock alteration, whereas P and Ti anomalies could be produced respectively by apatite and titanium oxides fractionation during the partial melting process.

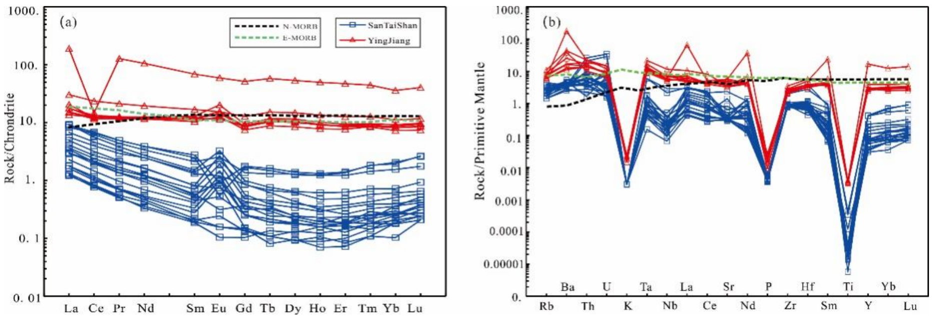

Figure 7. (**a**) Chondrite-normalized rare earth elements pattern. (**b**) Primitive mantle normalized trace elements pattern. Normalization and OIB values followed [30].

4.4. Sr–Nd Isotopic Geochemistry

In this study, six samples were selected from the SSPP rocks for analysis of the Sr–Nd isotopes. The test data are listed in Table S9. The initial Sr–Nd isotopic ratios and εNd(t) values for all the samples were calculated using the zircon U–Pb ages obtained in this study. The age of the depleted mantle model was calculated according to the DePaolo method [31,32], and all $(^{87}Sr/^{86}Sr)_i$ values were calculated during the crystallization of magma. The initial $^{87}Sr/^{86}Sr$ was 0.70910–0.71310, the initial $^{143}Nd/^{144}Nd$ was 0.512339–0.512874 and εNd(t) was −1.1–9.4. The calculated T_{DM} ages ranged from 610 to 942 Ma.

5. Discussion

5.1. Isotopic Chronology

The distribution of mafic and ultramafic rocks in western Yunnan is limited. The age of Yingjiang's ultramafic rocks has not been studied, and only a few studies have been reported on Santaishan's ultramafic rocks [13–19]. Many scholars believe that the Santaishan ultramafic rocks represent ophiolite, which is connected to the Bangong–Nujiang ophiolite belt to the north and the Myitkyina–Mogok ophiolite belt in Myanmar to the south [3,17,33,34]. Qi et al. [34] reported that the pyroxenite in Santaishan has zircon U–Pb ages of 183–185 Ma and believed that these ages represent the initial subduction of the Bangong–Nujiang Ocean. The ages of the SSPP rocks in this study varied from 186.2 to 190.5 Ma, which is close to those in previous research. In order to facilitate the comparison, we collected the chronological data of some ultramafic rocks (Table 1).

Table 1. Chronological data of ultramafic rocks in western Yunnan, Bangong–Nujiang, and Myitkyina–Mogok.

Tectonic Zone	Region	Sample	Zircon U/Pb Age (Ma)	Data Sources
Western Yunnan Ultrabasic Rocks	Santaishan	Serpentinized pyroxene peridotite	186.2 ± 2.3–190.5 ± 1.3	This article
	Yingjiang	Spinel hornblende dipyroxene	182.0 ± 1.4–183.7 ± 1.8	This article
	Santaishan	Pyroxene dikes	183.0 ± 1.7–185.0 ± 1.7	[34]
Bangong–Nujiang Ophiolite Belt	Bangong Lake	Gabbro	167.0 ± 1.4	[15]
	Rutog	Gabbro	169.0 ± 2.0	[35]
	Dongco	Gabbro	167.0 ± 2.0	[35]
	Dongqiao	Gabbro	187.0 ± 2.0	[35]
	Amdo	Gabbro	184.0 ± 2.0	[35]
	Dengqen	Gabbro	167.0 ± 1.4	[35]
Myitkyina–Magok Ophiolite Belt	Myitkyina	andesitic basalt	166.0 ± 3.0	[36]
	Myitkyina	Gabbro	177.0 ± 1.0	[36]
	Myitkyina	Olivine pyroxenolite	171.0 ± 2.0	[36]
	Myitkyina	Plagioclase granite	180.3 ± 1.6	[36]

Table 1. *Cont.*

Tectonic Zone	Region	Sample	Zircon U/Pb Age (Ma)	Data Sources
Myitkyina–Magok Ophiolite Belt	Myitkyina	Gabbro	171.6 ± 2.0	[37]
	Myitkyina	Diorite	173.0 ± 1.5	[37]
	Mogok	Plagioclase granite	176.0 ± 1.0	[33]

The Bangong–Nujiang ophiolite belt formed 167.0–187.0 Ma and was connected to the Greek and Albanian ophiolite belts to the west [15,34]. The ages of the Greek Vourinos ophiolite belt, the Pindos ophiolite belt and the Albanian Mirdita ophiolite belt are 179.0 Ma, 172.0–181.0 Ma and 160.0–174.0 Ma, respectively [38–40]. The Myitkyina–Mogok ophiolite belt in Myanmar that formed in the forearc subduction zone was the southward extension of the Bangong–Nujiang ophiolite belt [36,37,41–44]. Yang et al. proposed that the ages of gabbro and olivine pyroxenite in the Myitkyina ophiolite belt were 177.0 ± 1.0 Ma and 171.0 ± 2.0 Ma, respectively [36]. Liu et al. reported that the gabbro and diorite in the Myitkyina ophiolite belt had zircon U–Pb ages of 171.6 ± 2.0 Ma and 173.0 ± 1.5 Ma, respectively [37]. Wei et al. supposed that the plagioclase granite in the Mogok ophiolite belt was formed 176.0 ± 1.0 Ma [33]. As discussed above, the formation age of the Myitkyina–Mogok ophiolite belt is 171.6–177.0 Ma, which is similar to the Bangong–Nujiang ophiolite belt.

The studies above indicated that the ultramafic rocks in the western Yunnan have the same age as the western Tethys ophiolite belt, the Bangong–Nujiang ophiolite belt and the Myitkyina–Mogok ophiolite belt in Myanmar. The formation of these rocks was related to the evolution of the Neo-Tethys Ocean. Mo et al. [3] believed that the opening time of the Neo-Tethys Ocean was in the Late Triassic or earlier, and the subduction started at about 170 Ma. Shi et al. [15] studied the SSZ-type ophiolite in Bangong Lake and found that the maximum age of gabbro was 177.1 ± 1.4 Ma, suggesting that the subduction time of the Bangong–Nujiang Ocean was earlier than 177.1 Ma. The formation age of the Santaishan ultramafic rocks obtained in this study was 186.2–190.5 Ma, and the formation age of the Yingjiang ultramafic rocks was 182.0–183.7 Ma, indicating that the SSPP and the YHP were formed at the end of the Early Jurassic, belonging to the dissociation of the ancient united continent during Yanshanian's orogeny. This corresponds to the subduction of the Bangong–Nujiang Ocean, which was a branch of the Neo-Tethys Ocean.

A histogram of the age distribution of ultramafic rocks was made from these data (Figure 8). These rocks are mainly found in the Bangong–Nujiang ophiolite belt and the adjacent Neo-Tethys ophiolite belt. As can be seen in Figure 8a, the subduction of the Bangong–Nujiang Ocean in western Yunnan lasted for a long time, with ages ranging from 190.5 Ma to 160 Ma. The peak age appeared 170–180 Ma, indicating that the subduction process was most intense during this period. In view of the above (Figure 8b), the SSPP and the YHP are different products of subduction in the same period and tectonic environment.

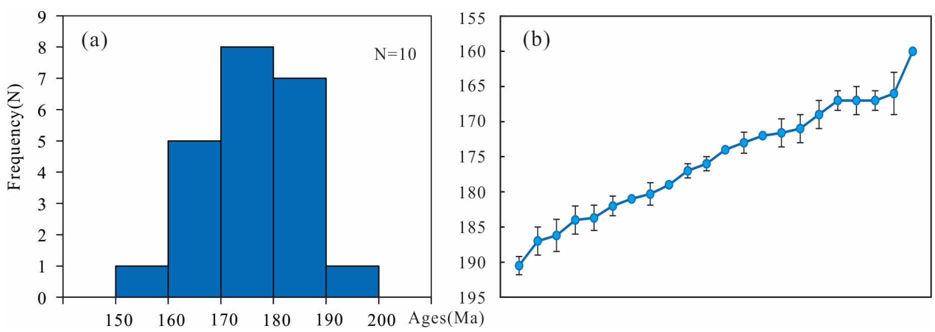

Figure 8. (**a**) Age distribution of the ultramafic rocks. (**b**) Summary of the ages for ultramafic rocks. The ages are listed in Table 1, data from Bangong–Nujiang ophiolite belt and the adjacent Neo-Tethys ophiolite belt.

5.2. Petrogenesis

The characteristics of the trace elements in the SSPP and the YHP are similar (Figure 7b), indicating that they may have derived from the same magma source. Both samples are enriched in LILEs such as Rb, Ba and Th, and depleted in HFSEs such as Ti, P and Nb, indicating that the rocks experienced some extent of crustal mixing or subduction melting/fluid metasomatism. The ratios of Na_2O/K_2O in the ultramafic rocks of Santaishan and Yingjiang were 0.20–0.22 and 0.15–0.27, respectively, indicating that the provenance of these two rocks may have been the mantle. In addition, the contents of highly compatible elements such as Cr, Ni and Co in the SSPP and the YHP were similar to those in the primitive mantle (Table 2) [45]. The solidification index (SI) can indicate the degree of magma differentiation and crystallization. Higher SI values indicate a lower degree of magma differentiation and vice versa. The SI values of the ultramafic rocks in Santaishan ranged from 76.24 to 85.26 (mean: 83.87) (Table S6), and those of the Yingjiang ultramafic rocks ranged from 52.67 to 59.75 (mean 56.99) (Table S2), indicating that the degree of differentiation of the ultramafic rocks in Santaishan is lower than that of Yingjiang ultramafic rocks. According to these findings, combined with isotopic chronology characteristics, the ultramafic rocks of Santaishan and Yingjiang come from the same mantle source and have experienced different degrees of evolution.

Table 2. Content of highly compatible elements. The Primitive Mantle values are from [46].

Region	Cr (ppm)	Ni (ppm)	Co (ppm)
Santaishan	1481.7–2911.4	724.2–2406.0	84.3–113.7
Yingjiang	806.6–1177.0	1597.6–2505.6	112.1–142.4
Primitive Mantle	300.0	2000.0	100.0

The depleted mantle is the remnant of the primitive mantle after partial melting, during which Si, Al, Ca, K, Na and other elements that tend to enter the liquid phase migrated out of the mantle source and into the magma. Compared with the primitive mantle, the depleted mantle lost K_2O, Na_2O, CaO, Al_2O_3, TiO_2 and other oxides, while the content of MgO increased significantly. The content of MgO in the mantle's peridotite can indicate the degree of partial melting in the magma source, and the higher the content of MgO, the higher the degree of partial melting [47]. The content of MgO in the Santaishan ultramafic rocks (32.94–39.20 wt.%) was much higher than that in the Yingjiang ultramafic rocks (22.89–27.20 wt.%), indicating that the source area of the Santaishan ultramafic rocks had a higher degree of partial melting than that of the Yingjiang ultramafic rocks. The ultramafic rocks in Santaishan had low total REE concentrations (1.14–10.65 ppm), relatively enriched LREEs and depleted HREEs, indicating a high degree of melting. The distribution pattern of REEs in the Yingjiang ultramafic rocks was flat, and the difference between LREEs and HREEs was not obvious, indicating that the degree of melting was low. In terms of mineral composition, no clinopyroxene was found in the Santaishan ultramafic rocks, indicating that the degree of partial melting of the magma source was higher than that of the Yingjiang ultramafic rocks, which contained clinopyroxene. In addition, the Ti content can also indicate the degree of partial melting, and its content is negatively correlated with the degree of melting. The Ti content in the Santaishan ultramafic rocks (0.001–0.110 wt.%) was significantly lower than that in the Yingjiang ultramafic rocks (0.91–1.11 wt.%), which indicated that the degree of partial melting of the Santaishan ultramafic rocks was higher than that of the Yingjiang ultramafic rocks. It is commonly believed that the content of incompatible elements is high in magma with a low degree of melting, and low in magma with a high degree of melting because these elements easily enter the molten rock. In the initial stage of melting, these elements tend to enter the molten rock; therefore, their proportion is larger when the degree of melting degree. With an increase in the degree of melting, the proportion of incompatible elements is diluted and reduced [48,49]. The content of incompatible elements in the Santaishan ultramafic rocks was considerably lower than in the Yingjiang ultramafic rocks, indicating that the degree of melting of the Santaishan ultramafic rocks is higher than that of the Yingjiang ultramafic rocks.

The influence of the magma's evolution is limited to the fractionation of isotopes. Thus, the Sr–Nd and Lu–Hf isotopes can be used to trace the magma source [30,50,51]. Generally speaking, a positive εHf(t) value indicates that the magma originated from the depleted mantle or newly formed crust, while a negative εHf(t) value indicates that the magma source was mainly the crustal materials or enriched mantle [52–54]. The εHf(t) values of the SSPP and the YHP were 11.2–13.8 and 3.5–6.9, respectively. The ultramafic rocks of Santaishan and Yingjiang are distributed between the depleted mantle and chondrite evolution lines in Figure 9a, indicating that the ultramafic rocks of Santaishan are mainly derived from the depleted mantle.

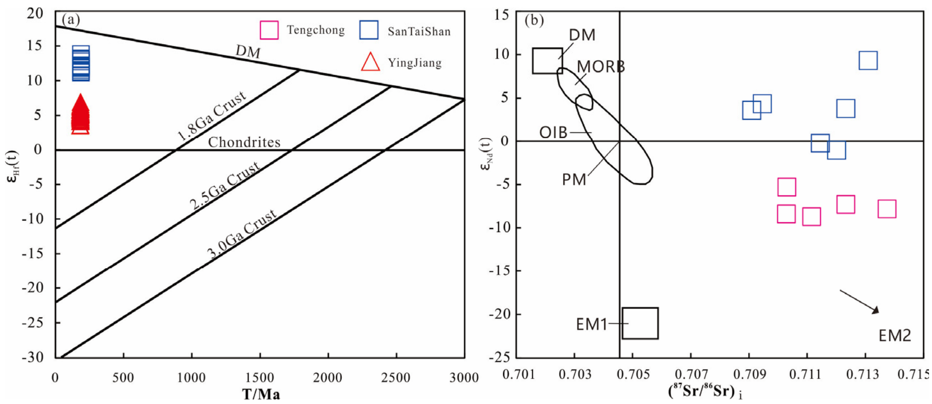

Figure 9. (**a**) Zircon T/Ma−εHf(t) diagram (modified from [55]). (**b**) $(^{87}Sr/^{86}Sr)_i$−εNd(t) diagram (modified from [56]). DM−depleted mantle, PM−primitive mantle, EM−enriched mantle, MORB−mid-ocean ridge basalt, OIB−ocean island basalts. Data are listed in Table S9.

The samples of the Yingjiang ultramafic rocks were close to the evolution line of the lower crust, indicating that the magma source may have been affected by crustal mixing. For mantle-derived magmas, if zircon originated from the uncontaminated depleted mantle, the zircon's crystallization age should be similar to the Hf model's age. The zircon Hf model's age (TDM1) of the YHP was 535–667 Ma, which is much older than the zircon crystallization age (183.6 Ma), suggesting that the magma source of Yingjiang ultramafic rocks may have been affected by mixing with crust materials.

Dupre and Allegre studied the MORB in the Indian Ocean. They found a mantle with abnormally enriched Sr isotopes ($(^{87}Sr/^{86}Sr)_i > 0.705$) in the Indian Ocean, which was called the Dupal anomaly [55–59]. In this study, the $(^{87}Sr/^{86}Sr)_i$ values of the SSPP were 0.7091–0.7123, indicating that the magma of the Santaishan ultramafic rocks originated from the Dupal anomaly's mantle domain. Zindler and Hart divided the mantle's end-members into four types, namely DM, HIMU, EM1 and EM2, and believed that additional mantle end-members evolved from the mixed evolution of these four basic end-members [60,61]. In the $(^{87}Sr/^{86}Sr)_i$–εNd(t) diagram (Figure 9b), the ultramafic samples from Santaishan were distributed in the depleted mantle area. Tengchong ultramafic rocks were found to have high $(^{87}Sr/^{86}Sr)_i$, and these isotopic data were recalculated to 190.5 Ma, and the $(^{87}Sr/^{86}Sr)_i$ value range was 0.7103~0.7137 (Table S9), which is consistent with the results of this study. However, εNd(t) values range from −5.3~−8.7, reflecting the heterogeneity of the mantle in the study area. Previous studies have shown that the Zhagabu mantle peridotites in the Yarlung Tsangpo ophiolite belt have large variability in both whole-rock and mineral compositions and may be derived from a heterogeneous mantle [62].

Island arc volcanic rocks are generally formed by partial melting of the mantle wedge's metasomatism by subduction fluids, which are usually depleted in HFSEs (such as Nb, Ta, Ti, etc.) [63]. The HFSEs mainly exist in the accessory minerals. When the oceanic crust subducted, the sediments and surface basalt were subducted along with them. Both the sediments and the surface basalts in the ocean are rich in fluid. With the subduction of the oceanic crust, dehydration led to precipitation of the active elements in the sediments and the surface basalts, while the elements such as Nb and Ta stayed in the accessory minerals. The released fluid migrated upward into the mantle wedge. During this process, metasomatism occurred between the fluid and the mantle wedge. At the same time, the solidus curve of the mantle's rocks decreased due to the increase in the water content in the mantle wedge, which resulted in partial melting of the mantle wedge and the enrichment of Rb, Sr, Th and other extremely active elements in the melt. However, the HFSEs, such as Nb and Ta, were relatively depleted [63–65]. Aqueous fluid can enhance the activity of LILEs, and the participation of fluid led to the relative enrichment of LILEs and the depletion of HFSEs [65]. The higher ($^{87}Sr/^{86}Sr)_i$ values (0.7091–0.7123) in the Santaishan ultramafic rocks indicate the characteristics of enrichment. Wang et al. analyzed the mineral components of ultramafic rocks in Santaishan using the single mineral electron probe method and believed that they were derived from 25%–35% partial melting of the depleted mantle [19]. Experimental petrology has proven that such a high degree of partial melting usually requires the participation of fluids in the subduction zone. The fluids normally come from the dehydration of the slab in-depth, and the migration of fluids is beneficial to the partial melting of the mantle wedge. In the Nb/YB-Th/Yb diagram (Figure 10a), the Santaishan ultramafic rocks had high Th/Yb ratios (1.12–25.31), and the samples were distributed away from the MORB–OIB evolutionary line. This indicated that the ultramafic rocks in Santaishan were influenced by more subduction components than the Yingjiang ultramafic rocks. In the Rb/Y-Nb/Y diagram (Figure 10b), the ultramafic rocks in Santaishan showed a trend of fluid metasomatism enrichment, indicating that the magma source was enriched by fluid metasomatism during subduction of the oceanic crust.

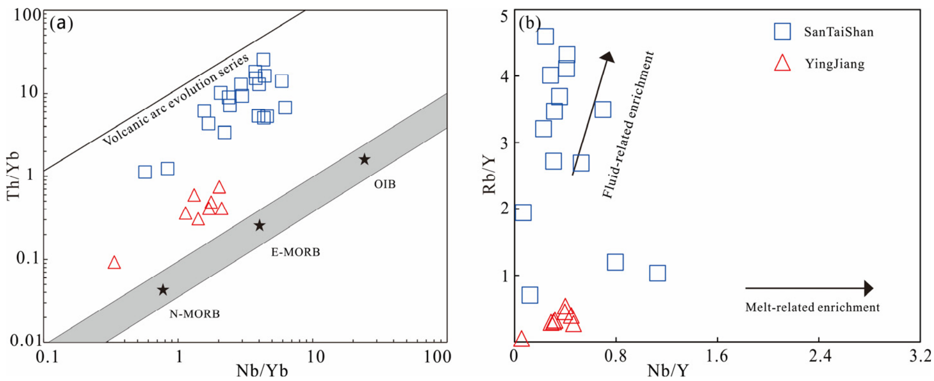

Figure 10. (**a**) Nb/Yb–Th/Yb diagram (modified from [66]); (**b**) Nb/Y–Rb/Y diagram (modified from [67]).

The Santaishan ultramafic rocks had a wide range of εNd(t) values (−1.1 to 9.4), which were similar to the modern MORB (7–12) from partial melting of the depleted mantle [68]. The Middle Jurassic basalts in this area (−0.6 to 2.6) [69] and the adjacent Myitkyina basalts (4.0–5.3) [40] also showed a similar distribution. The Sm–Nd isotopes of the Santaishan ultramafic rocks have been reported by previous studies [13,34]. In this study, these isotopic data were recalculated as 190.5 Ma, and the εNd(t) values ranged from −8.7 to 5.1 (Table S9). The results reflect the mantle's heterogeneity in the study area, which may be related to the crust–mantle recirculation of material during the early oceanic crust subduction [34,70–72]. The TDM of Nd mainly reflects the separation time of the crustal material or source rock from the depleted mantle, so the age distribution properties of the TDM can be used to trace the growth characteristics of the crust. The TDM1 ages of the Santaishan ultramafic rocks are concentrated in two phases: 942–909 Ma and 650–610 Ma. These two stages correspond to the formation of the Neoproterozoic Rodinia supercontinent (1000–900 Ma) and the Pan-African tectonic period of the Gondwana supercontinent (750–530 Ma), respectively. The Tengchong Block, located in the front of the subduction zone, experienced intense tectonic compression and transformation, and formed the heterogeneous mantle source region during the evolution of the Proto-Tethys Ocean. Under the subduction of the Neo-Tethys Ocean, this heterogeneous mantle partly melted and then formed the Santaishan and Yingjiang ultramafic rocks with different geochemical characteristics [34,73,74].

5.3. Tectonic Setting

The tectonic setting of the ultramafic rocks in Santaishan is controversial. In recent years, the viewpoints regarding the tectonic setting of ultramafic rocks in Santaishan can be divided into two types: the active continental margin [18,19,34] and the mid-ocean ridge setting [8,9,12,13]. Wang et al. believed that the peridotites in Santaishan had two tectonic settings: the mid-ocean ridge and the subducted continental margin [19]. Qi et al. believed that the serpentinized peridotite of Santaishan belonged to the SSZ-type ophiolite, which was formed in a fore-arc tectonic setting [34].

As shown in the Hf/3-TH-TA diagram (Figure 11a), the Santaishan ultramafic rocks were distributed in the CAB area, indicating the active continental margin setting, while the Yingjiang ultramafic rocks were mainly distributed in the WPA area, showing a within-plate setting [75].

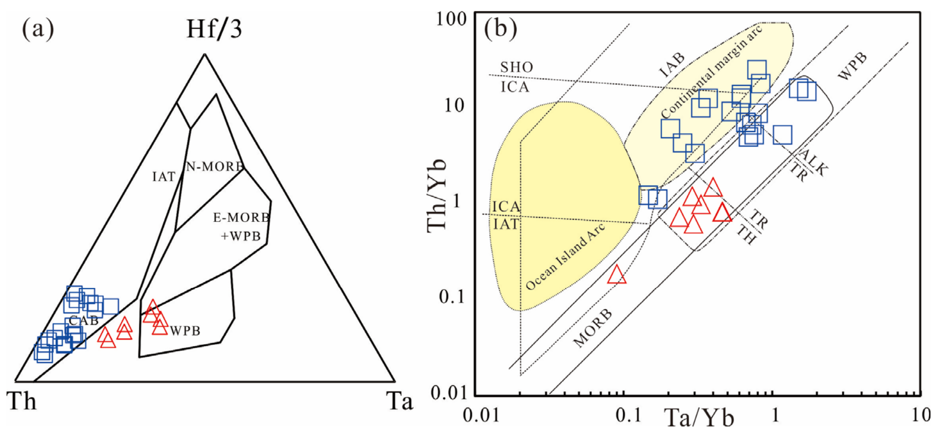

Figure 11. (**a**) Hf/3–Ta–Th diagram (modified from [76]); (**b**) Ta/Yb–Th/Yb diagram (modified from [65]). CAB: calc-alkaline basalt, WPB: within plate basalt, MORB: mid-ocean ridge basalt, IAT: island arc tholeiite, IAB: island arc basalt, ICA: island calcic alkali, SHO: Shoshone, TH: tholeiitic, TR: transition, ALK: alkali.

Moreover, in the Th/Yb-TA/Yb diagram (Figure 11b), the Santaishan ultramafic rocks were distributed in the continental margin arc area, and the Yingjiang ultramafic rocks were mainly distributed in the TH area, which has MORB characteristics. The active continental margin is the convergence margin of oceanic and continental plates formed by the subduction of oceanic plates, which is constantly accompanied by a series of volcanic arc magmatic assemblages. The dehydration of the lower inserted plate in the subduction zone leads to partial melting of the mantle wedge, and the HFSEs such as Nb, Ta and Ti are stable during dehydration, while the LILEs such as Rb, Sr and Ba are active, resulting in the enrichment of LILEs and depletion of HFSEs in the island arc or back-arc basin [77–79].

The retraction of the slab during subduction led to the upwelling of the asthenosphere, which, in turn, caused mantle convection and extension of the crust beneath the back-arc basin. Zhou et al. supposed that the friction heat generated by the subducting oceanic slab caused the mantle to overcome the viscous resistance and the diapir to rise [80]. The generation of a high heat flow caused the rapid extension of the surface, leading to the expansion of the back-arc crust. The emplacement of the melt formed by partial melting of the olive mantle induced the formation of a MORB-type low-potassium tholeiitic melt in the back-arc basin. When studying the Bangong–Nujiang ophiolite, Shi found that the SSZ-type ophiolite was characterized by relatively high MgO and SiO_2, and low Al_2O_3, CaO and TiO_2, and it did not contain clinopyroxene [81]. The MORB-type ophiolite was characterized by relatively low MgO and SiO_2, and high Al_2O_3, CaO and TiO_2 contents. The ultramafic rocks in Santaishan are characterized by high MgO (32.94–39.20 wt.%); low Al_2O_3 (0.35–9.23 wt.%), CaO (0.06–2.94 wt.%) and TiO_2 (0.001–0.110 wt.%); and no clinopyroxene, while the Yingjiang ultramafic rocks are characterized by relatively low MgO (22.89–27.20 wt.%), and high Al_2O_3 (3.83–4.59 wt.%), CaO (2.41–4.79 wt.%) and TiO_2 (0.91–1.11 wt.%) contents. These characteristics indicate that the Santaishan ultramafic rocks belong to the SSZ-type ophiolite and Yingjiang ultramafic rocks belong to the MORB-type ophiolite.

The petrographic characteristics showed that there is no plagioclase in the Santaishan ultramafic rocks, while plagioclase exists in the Yingjiang ultramafic rocks. In terms of the REE characteristics, the Eu anomaly (δEu = 0.26–3.85) in the Santaishan ultramafic rocks is obvious and that in the Yingjiang ultramafic rocks is unobvious (δEu = 0.98–1.80), indicating the significant fractional crystallization of plagioclase in the evolution of the magma of the Santaishan ultramafic rocks. Because rapid magma supply and rise are not conducive to the crystallization of plagioclase [82], the magma supply rate and rising velocity of the Santaishan ultramafic rocks were higher than those of the Yingjiang ultramafic rocks, which conforms to the trend of evolution from the Santaishan island arc to the Yingjiang back-arc basin [79].

Neumayr and Suess proposed that there was a trans-Eurasian ocean near the equator, namely the Tethys Ocean, according to the distribution of the fauna during the Jurassic [83,84]. The Tethys Ocean divided the continent into two parts: Laurasia in the north and Gondwana in the south. Since the concept of the Tethys Ocean was put forward, numerous scholars have gradually put their focus on the Tethys tectonic belt and enriched its global tectonic meanings [1–4,7,10,20,85–90]. Numerous scholars believe that the Tethys Ocean can be divided into at least two periods before the final collision between Gondwana and Laurasia, the Paleo-Tethys Ocean and the Neo-Tethys Ocean; some scholars believe that the Middle Tethys Ocean also existed [87,88]. During the Carboniferous to Permian period, there was a wedge-shaped oceanic basin in Pangaea with an east–west orientation. Mo et al. believed that this was the Paleo-Tethys Ocean, which triggered different understandings of the origin and evolution of the Tethys Ocean [3]. During the Middle to Late Triassic, the microcontinent between Lowa and Gondwana kept drifting; for example, the Sibumasu terrane and the Lhasa terrane separated from northern Gondwana in the Southern Hemisphere, drifted northward and spliced into the Paleo-Asian plate, eventually forming the giant Tethys orogenic belt [1–6]. The closure of the Tethys Ocean induced the collision of Laurasia and Gondwana and formed a giant orogenic belt stretching from the European Alps in the west to the Asian Himalayas in the east.

After comparing the geological and geophysical characteristics of the north and south sides of the Bangong–Nujiang suture zone, Pan et al. [91] suggested that the Bangong–Nujiang suture zone represented the northern boundary of the ancient continent of Gondwana. The Tengchong Block was located in the west of the Bangong–Nujiang suture zone and was a microplate that separated from the margin of Gondwana. During the Early Jurassic, the Tengchong Block and Baoshan Block were separated by the branch trough of the Bangong–Nujiang Ocean basin. The combination of ophiolite and volcanic arc magmatic rocks is a typical sign of subduction [92–94]. The Bangong–Nujiang ophiolite belt and the north Gangdisi ophiolite belt represent the same suture zone. The Bangong–Nujiang Oceanic crust subducted southward, while the Nujiang Ocean subducted westwards under the Tengchong Block in the Sanjiang area. Qiu et al. believed that the Bangong–Nujiang Ocean began to subduct southward in the Middle Jurassic and closed in the Early Cretaceous [14]. Mo et al. believed that the opening time of the Neo-Tethys Ocean should be the Late Triassic or earlier, and the subduction time started at about 170 Ma [3]. When Shi et al. studied the Bangong Lake ophiolite, they found that the maximum age of gabbro was 177 Ma, suggesting that the subduction of the Bangong–Nujiang Ocean was at least earlier than 177 Ma [15].

The Bangong–Nujiang Oceanic crust subducted beneath the Tengchong Block 190.5 Ma in the early Middle Jurassic and formed the Santaishan continental margin arc. The SSZ-type calc-alkaline pyroxene peridotite was formed under the dual effects of heating by plate compression and modified by the subduction fluid. With the continuous subduction of the Bangong–Nujiang Ocean, the slab retreated and further induced convection of the mantle and lithospheric extension. The crust in Yingjiang thinned, and the Yingjiang back-arc basin formed 183.7 Ma due to lithospheric extension. In this extensional setting, MORB-type tholeiitic dipyroxene was generated due to the decompression melting of the lithospheric mantle (Figure 12).

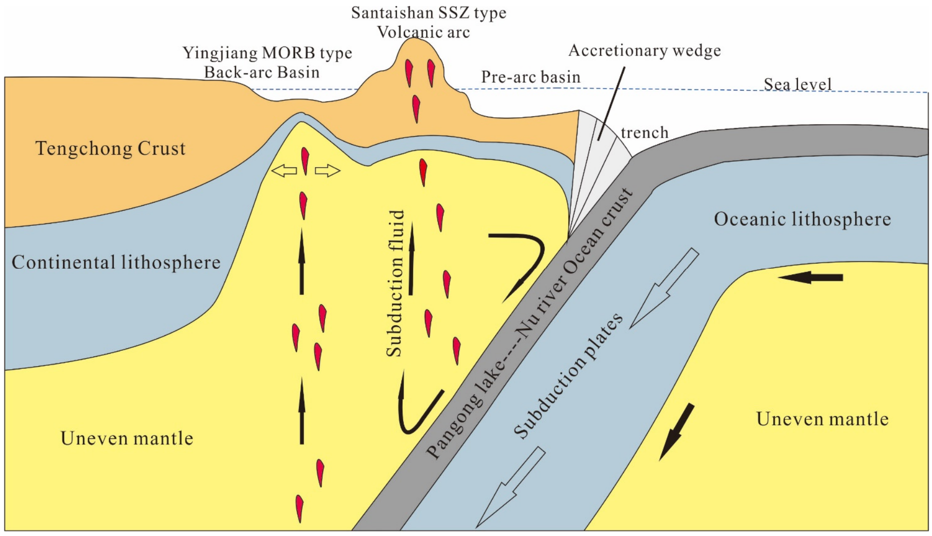

Figure 12. Tectonic setting model diagram of ultrabasic rock formation in Santaishan and Yingjiang.

6. Conclusions

Through a combination of geochronological, petrological and geochemical studies of the ultramafic rocks in western Yunnan, the following conclusions can be drawn.

The zircon U–Pb results show that the SSPP formed 186.2–190.5 Ma, and the YHP formed 182.0–183.7 Ma. Both correspond to the subduction of the Bangong–Nujiang Ocean branch.

The SSPP and YHP have similar trace elements; are enriched in LILEs such as Rb, Ba and Th; and are depleted in HFSEs such as Ti, P and Nb. The isotopic characteristics of Sr–Nd and Lu–Hf indicated that the SSPP and the YHP originated from a depleted mantle. The T_{DM1} age of SSPP indicated that the crustal material in the magma source may have come from the Neoproterozoic Rodinia supercontinent.

The subduction of the Bangong–Nujiang Ocean started 190.5 Ma, and the Tengchong Block was influenced by the subduction. The SSPP has SSZ-type characteristics, and the YHP shows MORB-type characteristics. The Santaishan area was in a continental margin arc environment, and the Yingjiang area was in an extensional setting where a back-arc basin formed.

Supplementary Materials: The following supporting information can be downloaded at: https://www.mdpi.com/article/10.3390/min13040536/s1, Table S1: Yingjiang ultramafic rock major element (%) and trace element (ppm); Table S2: Yingjiang ultramafic rock CIPW standard minerals (%); Table S3: Yingjiang ultramafic rock Zircon U–Pb contents; Table S4: Yingjiang ultramafic rock Lu–Hf isotopic compositions; Table S5: Santaishan ultramafic rock major element (%) and trace element (ppm); Table S6: Santaishan ultramafic rock CIPW standard minerals (%); Table S7: Santaishan ultramafic rock Zircon U–Pb contents; Table S8: Santaishan ultramafic rock Lu–Hf isotopic compositions; Table S9: Santaishan ultramafic rock Sr–Nd isotopic compositions.

Author Contributions: Writing—original draft preparation, H.L.; methodology, supervision and project administration, Y.C.; writing—review and editing, Z.S. All authors have read and agreed to the published version of the manuscript.

Funding: This research was funded by the National Natural Science Foundation of China (Grant Nos. 41972312, 41672329), the National Key Research and Development Project of China (Grant No. 2016YFC0600509) and the Project of China Geological Survey (Grant No. 1212011120341).

Data Availability Statement: The data presented in this study are available in supplementary material.

Acknowledgments: We are thankful to Silian Shen, Xiaosen Cao, Rong Yang and Xu Zhu for their assistance with sample collection and Binnan Zhao for her help with zircon U–Pb dating. We also thank Zhi Shang for his help with thin section observations. We are also indebted to the academic editor and three anonymous reviewers for their critical and constructive comments, which substantially improved an early version of the manuscript.

Conflicts of Interest: The authors declare no conflict of interest.

References

1. Zhu, R.X.; Zhao, P.; Zhao, L. Tectonic evolution and geodynamics of the Neo-Tethys Ocean. *Sci. China Earth Sci.* **2022**, *65*, 1–24. (In Chinese) [CrossRef]
2. Hou, Z.Q.; Zhang, H.R. Geodynamics and metallogeny of the eastern Tethyan metallogenic domain. *Ore Geol. Rev.* **2015**, *70*, 346–384. [CrossRef]
3. Mo, X.X.; Pan, G.T. From Tethys to Tibetan Plateau formation: Tectonic-magmatic event constraints. *Earth Sci. Front.* **2006**, *13*, 43–51. (In Chinese)
4. Deng, J.; Hou, Z.Q.; Mo, X.X.; Yang, L.Q.; Wang, C.M. Sanjiang Tethys composite orogeny and mineralization. *Miner. Depos.* **2010**, *29*, 37–42. (In Chinese)
5. Xu, Z.Q.; Yang, J.S.; Li, H.B.; Ji, S.C.; Zhang, Z.M.; Liu, Y. India-Asia collision geotectonics. *Acta Geol. Sin.* **2011**, *85*, 1–33. (In Chinese)
6. Ding, L.; Satybaev, M.; Cai, F.L.; Wang, H.Q.; Song, P.P.; Ji, W.Q.; Xu, Q.; Zhang, L.Y.; Qasim, M.; Baral, U. Processes of initial collision and suturing between India and Asia. *Sci. Sin. (Terrae)* **2017**, *47*, 293–309. (In Chinese) [CrossRef]
7. Wu, F.Y.; Wan, B.; Zhao, L.; Xiao, W.J.; Zhu, R.X. Tethyan geodynamics. *Acta Petrol. Sin.* **2020**, *36*, 1627–1674. (In Chinese)
8. Zhong, D.L.; Ding, L.; Liu, F.T.; Lu, J.H.; Zhang, J.J.; Ji, J.Q.; Chen, H. Multi-oriented and layered structures of lith osphere in orogenic belt and their effects on Cenozoic magmatism. *Sci. China Earth Sci.* **2000**, *43*, 122–133. [CrossRef]
9. Zhong, D.L.; Ding, L.; Zhang, J.J.; Ji, J.Q. Multi-Periodic Collisional Process between Indian and Asian Continents: A Case of Eastern Himalayan Syntaxis and Hengduan Mountains. *Earth Sci. Front.* **2000**, *S1*, 47–48.
10. Yin, A.; Harrison, T.M. Geologic Evolution of the Himalayan-Tibetan Orogen. *Earth Planet. Sci.* **2000**, *28*, 211–280. [CrossRef]
11. Zhou, K.K.; Mu, C.L.; Ge, X.Y.; Liang, W.; Chen, X.W.; Wang, Q.Y.; Wang, X.P. Lithofacies Paleogeography of the South China in Early Paleozoic and Its Reflection on Key Geological Problems. *Acta Sedimentol. Sin.* **2017**, *35*, 449–549. (In Chinese)
12. Zhang, Q.; Zhou, D.J.; Zhao, D.S. Wilson cycle of the PaleoTethyan Orogenic belt in western Yunnan: Record of magmatism and discussion on mantle process. *Acta Petrol. Sin.* **1996**, *12*, 17–28. (In Chinese)
13. Chu, Z.Y.; Wang, W.; Chen, F.K.; Wang, X.L.; Li, X.H.; Ji, J.Q. Os-Nd-Pb-Sr isotopic compositions of the Santaishan ultramafic rock in western Yunnan and its geological significances. *Acta Petrol. Sin.* **2009**, *25*, 3221–3228, (In Chinese with English Abstract).
14. Qiu, R.Z.; Cai, Z.Y.; Li, J.F. Boni nite of ophiolite belts in western QingHai-Tibet plateau and it's Geological implication. *Geoscience* **2004**, *3*, 305–308. (In Chinese)
15. Shi, R.D. Age of SSZ ophiolite in Bangong: Constraintion on formation age of Bangong-Nujiang suture. *Chin. Sci Bull.* **2007**, *52*, 223–227. (In Chinese)
16. Chen, Y.Q.; Li, G.J.; Qin, L.X.; Lu, Y.X.; Jiang, C.X. Geochronology and geochemistry of Cretaceous–Eocene granites, Tengchong Block (SW China): Petrogenesis and implications for Mesozoic-Cenozoic tectonic evolution of Eastern Tethys. *Geosci. Front.* **2022**, *13*, 220–242. [CrossRef]
17. Zhong, D.L.; Ding, L.; Zhang, J.J.; Ji, J.Q. Study of Orogenic Belts in China: Retrospects and Prospects. *Geol. Rev.* **2002**, *48*, 147–152, (In Chinese with English Abstract).
18. Liu, B.P.; Feng, Q.L.; Chonglakmani, C.; Helmcke, D. Framework of PaleoTethyan archipelago ocean of western Yunnan and it's elongation towards north and south. *Earth Sci. Front.* **2002**, *9*, 161–170, (In Chinese with English Abstract).
19. Wang, Y.X.; Wang, G.H.; Yuan, G.L.; Wang, X.J.; Lu, Y.; Lin, Y. Tectonic genesis of the Santaishan peridotites in western Yunnan and its geological significance: Evidence from geology, mineralogy and petrogeochemistry. *Earth Sci. Front.* **2018**, *25*, 138–156, (In Chinese with English Abstract).
20. Zhou, S.M.; Wang, Q.F.; Li, G.J. Geochemistry, zircon U-Pb geochronology from the Late Triassic syenogranite in Lianghe area, Tengchong Block, and their geological implications. *Acta Petrol. Sin.* **2018**, *34*, 1359–1375. (In Chinese)
21. Chen, X.C.; Hu, R.Z.; Bi, X.W.; Zhong, H.; Lan, J.B.; Zhao, C.H.; Zhu, J.J. Petrogenesis of metaluminous A-type granitoids in the Tengchong-Lianghe tin belt of southwestern China: Evidences from zircon U-Pb ages and Hf-O isotopes, and whole-rock Sr-Nd isotopes. *Lithos* **2015**, *212*, 93–110. [CrossRef]
22. Cong, F.; Lin, S.L.; Zou, G.F.; Xie, T.; Li, Z.H.; Tang, F.W.; Peng, Z.M. Geochronology and petrogenesis for the protolith of biotite plagioclase gneiss at Lianghe, western Yunnan. *Acta Geol. Sin.* **2011**, *85*, 870–880. [CrossRef]

23. Liu, Y.S.; Gao, S.; Hu, Z.C.; Gao, C.G.; Zong, K.Q.; Wang, D.B. Continental and oceanic crust recycling-induced melt-peridotite interactions in the Trans-North China Orogen: U-Pb dating, Hf isotopes and trace elements in zircons from mantle xenoliths. *J. Petrol.* **2010**, *51*, 537–571. [CrossRef]
24. Ludwig, K.R. *ISOPLOT 3.0: A Geochronological Toolkit for Microsoft Excel*; Special Publication No. 4; Berkeley Geochronology Center: Berkeley, CA, USA, 2003; Volume 4, pp. 1–71.
25. Wu, F.Y.; Li, X.H.; Zheng, Y.F.; Gao, S. Lu-Hf isotopic systematics and their applications in petrology. *Acta Petrol. Sin.* **2007**, *23*, 185–220, (In Chinese with English Abstract).
26. Gao, S.; Liu, X.M.; Yuan, H.L.; Hattendorf, B.; Günther, D.; Chen, L.; Hu, S. Determination of Forty Two Major and Trace Elements in USGS and NIST SRM Glasses by Laser Ablation-Inductively Coupled Plasma-Mass Spectrometry. *Geostand. Newsl.* **2002**, *26*, 181–196. [CrossRef]
27. Yan, Q.R.; Wang, Z.Q.; Liu, S.W. Opening of the Tethys in southwest China and its significance to the breakup of East Gondwanaland in late Paleozoic: Evidence from SHRIMP U-Pb zircon analyses for the Garzê ophiolite block. *Chin. Sci. Bull.* **2005**, *50*, 256–264. [CrossRef]
28. Le Bas, M.J.; Le Maitre, R.W.; Streckeisen, A.; Zanettin, B. A chemical classification of volcanic rocks based on the total alkali-silica diagram. *J. Petrol.* **1986**, *27*, 745–750. [CrossRef]
29. Miyashiro, A. Volcanic rock series in island arc and active continental margins. *Am. J. Sci.* **1974**, *274*, 321–355. [CrossRef]
30. Sun, S.-S.; McDonough, W.F. Chemical and isotopic systematics of oceanic basalts: Implications for mantle composition and processes. *Geol. Soc. Lond. Spec. Publ.* **1989**, *42*, 313–345. [CrossRef]
31. DePaolo, D.J. Trace element and isotopic effects of combined wallrock assimilation and fractional crystallisation. *Earth Planet. Sci. Lett.* **1981**, *53*, 189–202. [CrossRef]
32. DePaolo, D.J.; Linn, A.M.; Schuberi, G. The continental crust age distribution: Methods of determining mantle separation ages from Sm-Nd isotopic data and implication to the southwestern United States. *Geophys. Res.* **1991**, *96*, 2071–2088. [CrossRef]
33. Wei, C.; Peng, T.P.; Fan, W.M.; Zhang, J.Y.; Gao, J.F.; Dong, X.H.; Ling, X.R.; Chen, L.L. Petrological and mineralogical chemistry of mantle peridotites from the Myitkyina-Mogok ophiolitic belt (Myanmar) and its tectonic significance. *Geochica* **2018**, *47*, 612–626, (In Chinese with English Abstract).
34. Qi, X.X.; Sheng, H.; Wei, C.; Ren, Y.F.; Cai, Z.H.; Ji, F.B.; Liang, F.H.; Liu, X.F. Longlin-Ruili subduction-accretionary complex belt in the southeastern Gaoligong orogen, and its relationship with the evolution of the Meso-Tethyan Ocean. *Acta Petrol. Sin.* **2021**, *37*, 3067–3094, (In Chinese with English Abstract).
35. Wang, B.D.; Wang, L.Q.; Chung, S.L.; Chen, J.L.; Yin, F.G.; Liu, H.; Li, X.B.; Chen, L.K. Evolution of the Bangong-Nujiang Tethyan ocean: Insights from the geochronology and geochemistry of mafc rocks within ophiolites. *Lithos* **2016**, *245*, 18–33. [CrossRef]
36. Yang, J.S.; Xu, Z.Q.; Duan, X.D.; Li, J.; Xiong, F.H.; Liu, Z.; Cai, Z.H.; Li, H.Q. Discovery of a Jurassic SSZ ophiolite in the Myitkyina region of Myanmar. *Acta Pet. Sin.* **2012**, *28*, 1710–1730, (In Chinese with English Abstract).
37. Liu, C.Z.; Chung, S.L.; Wu, F.Y.; Zhang, C.; Xu, Y.; Wang, J.G.; Chen, Y.; Shun, G. Tethyan suturing in Southeast Asia: Zircon U-Pb and Hf-O isotopic constraints from Myanmar ophiolites. *Geology* **2016**, *44*, 311–314. [CrossRef]
38. Robertson, A.H.F. Overview of the genesis and emplacement of Mesozoic ophiolites in the Eastern Mediterranean Tethyan region. *Lithos* **2002**, *65*, 1–67. [CrossRef]
39. Flower, M.F.J. Ophiolites, historical contingency, and the Wilson Cycle. The Ophiolite Concept and the Evolution of Geological Thought (ads, Dilek Y and Newcomb S). *Geol. Soc. Am. Spec. Pap.* **2003**, *373*, 111–135.
40. Dimo-Lahitte, A.; Monte, P.; Vergely, P. Metamorphic soles from the Albanian ophiolites: Petrology, $^{40}Ar/^{39}Ar$ geochronology, and geodynamic evolution. *Tectonics* **2001**, *20*, 78–96. [CrossRef]
41. Mitchell, A.; Chung, S.L.; Oo, T.; Lin, T.H.; Hung, C.H. Zircon U-Pb ages in Myanmar: Magmatic-metamorphic events and the closure of a Neo-Tethys Ocean? *J. Asian Earth Sci.* **2012**, *56*, 1–23. [CrossRef]
42. Searle, M.P.; Morley, C.K.; Waters, D.J.; Gardiner, N.J.; Htun, U.K.; Nu, T.T.; Robb, L.J. Tectonic and metamorphic evolution of the Mogok Metamorphic and Jade Mines belts and ophiolitic terranes of Burma (Myanmar). *Geol. Soc. Mem.* **2017**, *48*, 261–293. [CrossRef]
43. Gardiner, N.J.; Searle, M.P.; Morley, C.K.; Robb, L.J.; Whitehouse, M.J.; Roberts, N.M.W.; Kirkland, C.L.; Spencer, C.J. The crustal architecture of Myanmar imaged through zircon U-Pb, Lu-Hf and O isotopes: Tectonic and metallogenic implications. *Gondwana Res.* **2018**, *62*, 27–60. [CrossRef]
44. Ridd, M.F.; Crow, M.J.; Morley, C.K. The role of strike-slip faulting in the history of the Hukawng Block and the Jade Mines Uplift, Myanmar. *Proc. Geol.* **2019**, *130*, 126–141. [CrossRef]
45. Gao, S.; Luo, T.C.; Zhang, B.R.; Zhang, H.F.; Han, Y.W.; Zhao, Z.D. Structure and composition of the earth's crust in eastern China. *Sci. China (Ser. D)* **1999**, *29*, 204–214. (In Chinese)
46. Sun, S.-S. McDonough, The composition of the Earth. *Chem. Geol.* **1995**, *120*, 223–253.
47. Xu, Y.G.; Chung, S.L. The Emeishan large Igneous Province: Evidence for mantle plume activity and melting conditions. *Geochimica* **2001**, *1*, 1–10, (In Chinese with English Abstract).
48. Niu, Y. Mantle Melting and Melt Extraction Processes beneath Ocean Ridges: Evidence from Abyssal Peridotites. *J. Petrol.* **1997**, *38*, 1047–1074. [CrossRef]
49. Parkinson, J.; Pearce, J.A. Peridotites from the Izu–Bonin–Mariana Forearc (ODP Leg 125): Evidence for Mantle Melting and Melt–Mantle Interaction in a, Supra-Subduction Zone Setting. *J. Petrol.* **1998**, *39*, 1577–1618. [CrossRef]

50. Mckenzie, D.; O'nions, R.K. Partial Melt Distributions from Inversion of Rare Earth Element Concentrations. *J. Petrol.* **1991**, *5*, 1021–1091. [CrossRef]
51. Wu, F.Y.; Sun, D.Y.; Li, H.M.; Jahn, B.M.; Wilde, S. A-type granites in northeastern China: Age and geochemical constraints on their petrogenesis. *Chem. Geol.* **2002**, *187*, 143–173. [CrossRef]
52. Zhu, D.C.; Zhao, Z.D.; Niu, Y.L.; Mo, X.X.; Chung, S.L.; Hou, Z.Q.; Wang, L.Q.; Wu, F.Y. The Lhasa Terrane: Record of a microcontinent and its histories of drift and growth. *Earth Planet. Sci. Lett.* **2011**, *301*, 241–255. [CrossRef]
53. Zhu, D.C.; Mo, X.X.; Wang, L.Q.; Zhao, Z.D.; Niu, Y.L.; Zhou, C.Y.; Yang, Y.H. Petrogenesis of highly fractionated I-type granites in the Chayu area of eastern Gangdese, Tibet: Constraints from zircon U-Pb geochronology, geochemistry and Sr-Nd-Hf isotopes. *Sci. Sin. (Terrae)* **2009**, *39*, 833–848. (In Chinese)
54. Zhu, D.C.; Zhao, Z.D.; Pan, G.T.; Lee, H.Y.; Kang, Z.Q.; Liao, Z.L.; Wang, L.Q.; Li, G.M.; Dong, G.C.; Liu, B. Early cretaceous subduction-related adakite-like rocks of the Gangdese Belt, southern Tibet: Products of slab melting and subsequent melt–peridotite interaction? *J. Asian Earth Sci.* **2009**, *34*, 298–309. [CrossRef]
55. Tang, D.M.; Qin, K.Z.; Li, C.S.; Qi, L.; Su, B.X.; Qu, W.J. Zircon dating, Hf–Sr–Nd–Os isotopes and PGE geochemistry of the Tianyu sulfide-bearing mafic–ultramafic intrusion in the Central Asian Orogenic Belt, NW China. *Lithos* **2011**, *126*, 84–98. [CrossRef]
56. Shang, Z.; Chen, Y.Q. Zircon U–Pb Geochronology, Geochemistry and Geological Significance of the Anisian Alkaline Basalts in Gejiu District, Yunnan Province. *Minerals* **2020**, *11*, 1030. [CrossRef]
57. Allegre, C.J.; Brevart, O.; Dupre, B.; Minster, J.-F. Isotopic and Chemical Effects Produced in a Continuously Differentiating Convecting Earth Mantle. *Philos. Trans. R. Soc. A Math. Phys. Eng. Sci.* **1980**, *1431*, 447–477.
58. Allegre, C.J.; Dupre, B.; Negrel, P.; Gaillardet, J. Sr-Nd-Pb isotope systematics in Amazon and Congo River systems: Constraints about erosion processes. *Chem. Geol.* **1996**, *1*, 93–112. [CrossRef]
59. Hamelin, B.; Dupre, B.; Allègre, C.J. Lead-strontium-neodymium isotopic data of Indian Ocean ridges: New evidence of large-scale mapping of mantle heterogeneities. *Earth Planet. Sci. Lett.* **1986**, *76*, 288–298. [CrossRef]
60. Zindler, A.; Hart, S. Chemical Geodynamics. *Annu. Rev. Earth Planet. Sci.* **1986**, *14*, 493–571. [CrossRef]
61. Hart, S.R. Heterogeneous mantle domains: Signatures, genesis and mixing chronologies. *Earth Planet. Sci. Lett.* **1988**, *3*, 273–296. [CrossRef]
62. Zhang, Z.; Liu, T.; Liu, C.Z.; Zhang, C.; Wu, F.Y. The heterogeneous mantle massif in south Tibetan ophiolites and its implication for the tectonic evolution of Neo-Tethys. *Lithos* **2022**, *424–425*, 106761. [CrossRef]
63. Zhang, Z.C.; Yan, S.H.; Chen, B.L.; Zhou, G.; He, Y.K.; Chai, F.M.; He, L.X.; Wan, Y.S. SHRIMP zircon U-Pb dating for subduction-related granitic rocks in the northern part of east Junggar, Xinjiang. *Chin. Sci. Bull.* **2006**, *51*, 952–962, (In Chinese with English Abstract). [CrossRef]
64. Akiko, S.; Mineo, I.; Ichiro, K. Beryllium isotopic systematics in island arc volcanic rocks from northeast Japan: Implications for the incorporation of oceanic sediments into island arc magmas. *Chem. Geol.* **2016**, *443*, 158–172.
65. Adam, M.M.A.; Lv, X.B.; Fathy, D.; Rahman, A.R.A.; Ali, A.A.; Mohammed, A.S.; Farahat, E.S.; Sami, M. Petrogenesis and tectonic implications of Tonian island arc volcanic rocks from the Gabgaba Terrane in the Arabian-Nubian Shield (NE Sudan). *J. Asian Earth Sci.* **2022**, *223*, 1367–9120. [CrossRef]
66. Xu, Y.G. Roles of Thermo-mechanic and Chemical Erosion in Continental Lithospheric Thinning. *Bull. Mineral. Petrol. Geochem.* **1999**, *1*, 3–7, (In Chinese with English Abstract).
67. Pearce, J.A.; Cann, J.R. Tectonic setting of basic volcanic rocks determined using trace element analyses. *Earth Planet. Sci. Lett.* **1973**, *19*, 290–300. [CrossRef]
68. Wu, K. The Role of Melts/Fluids in Subduction Zones: Implications from Serpentinization and Fluxing/Metasomatic Processes. Ph.D. Thesis, University of Chinese Academy of Sciences, Beijing, China, May 2018. (In Chinese with English Abstract).
69. Handler, M.R.; Bennett, V.C.; Carlson, R.W. Nd, Sr and Os isotope systematics in young, fertile spinel peridotite xenoliths from northern Queensland, Australia: A unique view of depleted MORB mantle? *Geochim. Cosmochim. Acta* **2005**, *69*, 5747–5763. [CrossRef]
70. Castillo, P.R.; Liu, X.J.; Scarsi, P. The geochemistry and Sr-Nd-Pb isotopic ratios of high $^3He/^4He$ Afar and MER basalts indicate a significant role of the African superplume in EARS magmatism. *Lithos* **2020**, *376–377*, 105791. [CrossRef]
71. Delavault, H.; Chauvel, C.; Thomassot, E.; Devey, C.W.; Dazas, B. Sulfur and lead isotopic evidence of relic Archean sediments in the Pitcairn mantle plume. *Proc. Natl. Acad. Sci. USA* **2016**, *113*, 12952–12956. [CrossRef]
72. Nelson, W.R.; Hanan, B.B.; Graham, D.W.; Shirey, S.B.; Yirgu, G.; Ayalew, D.; Furman, T. Distinguishing plume and metasomatized lithospheric mantle contributions to post-flood basalt volcanism on the southeastern Ethiopian Plateau. *J. Petrol.* **2019**, *60*, 1063–1094. [CrossRef]
73. Yang, J.S.; Wu, W.W.; Lian, D.Y.; Rui, H.C. Peridotite, chromitites and diamonds in ophiolites. *Nat. Rev. Earth Environ.* **2021**, *2*, 198–212, (In Chinese with English Abstract). [CrossRef]
74. Qi, X.X.; Shen, H.; Ren, Y.F.; Wei, C.; Cai, Z.H.; Zhang, C.; Ji, F.B.; Liang, F.H. Early Cretaceous volcanism in the northwestern Gaoligong orogen and its relationship with subduction of the Nujiang Ocean: Evidence from geochemistry, zircon U-Pb dating and Hf isotopic compositions of rhyolites. *Acta Petrol. Sin.* **2020**, *36*, 2946–2962, (In Chinese with English Abstract).
75. Hollocher, K.; Robinson, P.; Terry, M.P.; Walsh, E. Application of major- and trace-element geochemistry to refine U-Pb zircon, and Sm/Nd or Lu/Hf sampling targets for geochronology of HP and UHP eclogites, Western Gneiss Region, Norway. *Am. Mineral.* **2007**, *11*, 1919–1924. [CrossRef]
76. Wood, D.A. The application of a Th-Hf-Ta diagram to problems of tectonomagmatic classification and to establishing the nature of crustal contamination of basaltic lavas of the British Tertiary Volcanic Province. *Earth Planet. Sci. Lett.* **1980**, *50*, 11–30. [CrossRef]

77. Tatsumi, Y. Migration of fluid phases and genesis of basalt magmas in subduction zones. *J. Geophys. Res. Solid Earth* **1989**, *94*, 4697–4707. [CrossRef]
78. McCulloch, M.T.; Gamble, J.A. Geochemical and geodynamical constraints on subduction zone magmatism. *Earth Planet. Sci. Lett.* **1991**, *102*, 358–374. [CrossRef]
79. Class, C.; Miller, D.M.; Goldstein, S.L.; Langmuir, C.H. Distinguishing melt and fluid subduction components in Umnak Volcanics, Aleutian Arc. *Geochem. Geophys. Geosyst.* **2013**, *1*, 1–28. [CrossRef]
80. Zhou, S.Q.; Huang, H.P.; Lin, C.S.; Li, C.G. The basin types and reservoir forming condition of circum-Pacific active margins. *Offshore Oil* **2006**, *4*, 13–17, (In Chinese with English Abstract).
81. Shi, R.D. Recognition of the Bangong Lake MOR-and SSZ-type Ophiolites in the Northwestern Tibet Plateau and its Tectonic Significance. Ph.D. Thesis, Chinese Academy of Geological Sciences, Beijing, China, May 2005. (In Chinese with English Abstract).
82. Zellmer, G.F.; Rubin, K.H.; Dulski, P.; Iizuka, Y.; Goldstein, S.L.; Perfit, M.R. Crystal growth during dike injection of Rbasaltic melts: Evidence from preservation of local Sr disequilibria in plagioclase. *Contrib. Mineral. Petrol.* **2011**, *161*, 153–173. [CrossRef]
83. Neumayr, M. Die geographische Verbreitung der Juraformation. *Denkschr Akad Wiss Wien Math-Nat. Cl* **1885**, *15*, 57–114.
84. Suess, E. Are great ocean depths permanent? *Nat. Sci.* **1893**, *2*, 180–187.
85. Stöcklin, J. Structural history and tectonics of Iran: A review. *AAPG Bull.* **1968**, *52*, 1229–1258.
86. Stöcklin, J. Northern Iran: Alborz Mountains. *Geol. Soc. Lond. Spec. Publ.* **1974**, *4*, 213–234. [CrossRef]
87. Sengör, A.M.C. Mid-Mesozoic closure of Permo-Triassic Tethys and its implications. *Nature* **1979**, *279*, 590–593. [CrossRef]
88. Sengör, A.M.C. Tectonics of the Tethysides: Orogenic collage development in a collisional setting. *Annu. Rev. Earth Planet Sci.* **1987**, *15*, 213–244. [CrossRef]
89. Searle, M.; Cox, J. Tectonic setting, origin, and obduction of the Oman ophiolite. *Geol. Soc. Am. Bull.* **1999**, *111*, 104–122. [CrossRef]
90. Stampfli, G.M.; Borel, G.D. A plate tectonic model for the Paleozoic and Mesozoic constrained by dynamic plate boundaries and restored synthetic oceanic isochrons. *Earth Planet Sci. Lett.* **2002**, *196*, 17–33. [CrossRef]
91. Pan, G.T.; Zhu, D.C.; Wang, L.Q.; Liao, Z.L.; Geng, Q.R.; Jiang, X.S. Bangong Lake-Nu River suture zone-The northern boundary of Gondwanaland: Evidence from geology and geophysics. *Earth Sci. Front.* **2004**, *4*, 371–382, (In Chinese with English Abstract).
92. Zhang, Q.; Qian, Q.; Wang, Y. Rock Asse mblages of Ophiolites and Magmatism beneath Oceanic Ridges. *Acta Petrol. Mineral.* **2000**, *19*, 1–7, (In Chinese with English Abstract).
93. Mo, X.X.; Deng, J.F.; Dong, F.L.; Yu, X.H.; Wang, Y.; Zhou, S.; Yang, W.G. Volcanic Petrotectonic Assemblages in Sanjiang Orogenic Belt SW China and Implication for Tectonics. *Geol. J. China Univ.* **2001**, *2*, 121–138, (In Chinese with English Abstract).
94. Li, W.C.; Yin, G.H.; Lu, Y.X.; Wang, Y.B.; Yu, H.J.; Cao, X.M.; Zhang, S.Q. Delineation of Hongshan-Shudu ophiolite mélange in Geza volcanic magmatic arc and its significance southwest "Jinsha-Lancang-Nu rivers". *Acta Petrol. Sin.* **2010**, *26*, 1661–1671. (In Chinese with English Abstract)